Supporting Information

Anticevic et al. 10.1073/pnas.1208494109

SI Text

Subjects. All subjects provided informed consent approved by Yale University's Institutional Review Board. We recruited 58 subjects from the local community by advertisement to participate in the present study. Of those, 40 were eligible and entered the study. Nineteen healthy, neurologically and psychiatrically intact right-handed volunteers (10 male) with a mean ± SD age of 27.5 ± 6.3 y completed the study. Subjects withdrew for the following reasons: (*i*) necessary time commitment for this study ($n = 6$); (*ii*) strong phenomenological response to ketamine ($n = 4$); (*iii*) noncompliance with the protocol procedures ($n = 1$); (*iv*) minor adverse events ($n = 3$); (*v*) concerns over taking ketamine ($n = 3$); and (*vi*) rescreened ($n = 3$). One subject's fMRI data were unusable. Subjects were first screened using an initial telephone interview and underwent a subsequent diagnostic interview using the Structured Clinical Interview for the DSM-IV (SCID) (1). Subjects also underwent a physical examination by a physician and a drug screen. Subjects were excluded for any psychiatric or major physical illness [e.g., severe endocrine disorder (Cushing syndrome, lupus), heart disorder (past history of heart attacks, angina), or other major systemic medical conditions (kidney, multiple sclerosis, cerebral palsy, blindness, serious physical disability] or chronic/acute condition including any managed by medication, head injury, history of neurological symptoms, loss of consciousness, drug or alcohol dependence, and smoking, as well as family history of psychiatric history and alcohol problems.

Overall Experimental Design. Present data were collected as one part of a larger study examining effects of a positive allosteric modulator (PAM) of the metabotropic glutamate receptor (mGluR) on effects of ketamine. Effects of mGluR were not relevant for the reported effects of the current study but will be reported in subsequent manuscripts. We used a double-blind, placebo-controlled, randomized, within-subjects design. Subjects completed three sessions before which they were randomly assigned to pretreatment of different dose of mGluR PAM [0 mg (placebo), 50 mg, or 180 mg], which they received a day before the scan. The aim of this aspect of the design was to ascertain whether pretreatment with an mGluR PAM exerted an ameliorative effect on the glutamatergic deficit induced via NMDA receptor blockade produced by ketamine administration, motivated by prior results in patients (2). mGluR PAM pretreatment did not alter any reported effects (i.e., behavior, fMRI activation, functional connectivity, or relationship with symptoms) in the context of the present WM task. Therefore, for all reported analyses, we collapsed across the pretreatment condition to increase statistical power and we focused on ketamine-related WM effects explicitly. The order of pretreatment visits was counterbalanced across subjects and spaced by at least 2 wk.

Infusion Protocol. As done in our prior work (3), subjects were administered racemic ketamine (1 mg/mL) i.v. via initial bolus (0.23 mg/kg over 1 min), followed by subsequent continuous target-controlled infusion (0.58 mg/kg over 1 h; plasma target, 200 ng/mL) using a computerized pump (Sigma Spectrum pump; P/N-35162). This resulted in achieved plasma concentrations of 183 ng/mL (~0.77 μM) using the pharmacokinetic parameters of a three-compartment model (4).

Clinical Measures. Subjects underwent clinical ratings the morning before the scan and immediately following ketamine infusion: (*i*) the Clinician-Administered Dissociative States Scale (CADSS) (5); and (*ii*) the Positive and Negative Syndrome Scale (PANSS), which is designed to assess positive, negative, and general aspects of schizophrenia psychopathology (6). These scales are extensively validated, standardized, and frequently used to assess schizophrenia symptoms.

Behavioral Results. As noted, the overall design involved two load levels and three levels of pretreatment with an mGluR PAM. No term involving either pretreatment or load interacted with effects of ketamine. Therefore, we report overall effect of ketamine on WM relative to the control task (Fig. 1*C* and Fig. S1). We computed a repeated-measures ANOVA with task condition (WM vs. control) × infusion (ketamine vs. placebo) as factors. Results revealed a highly significant main effect of task condition [$F(1,18) = 48.56$; $P < 0.0001$], as well as a task condition × infusion interaction [$F(1,18) = 29.14$; $P < 0.0001$]. Reaction time (RT) results revealed a highly significant main effect of task condition [$F(1,18) = 43.79$; $P < 0.0001$]. No other terms were significant for RT. For simplicity, we computed a percent drop in accuracy following ketamine vs. placebo for each subject, across both control and WM tasks separately. These effects are presented in the main text to facilitate visual inspection of ketamine effects on WM (Fig. 1*C*).

fMRI Acquisition. Functional images were acquired using an asymmetric spin-echo, echo-planar sequence maximally sensitive to blood oxygenation level-dependent (BOLD) contrast (T2*) [repetition time (TR), 1500 ms; echo time (TE), 30 ms; field of view (FOV), 200 mm; flip, 80°; voxel size, 3.125 × 3.125 × 5 mm], with 24 axial slices parallel to the AC-PC line. All functional acquisitions lasted 4.15 min and produced 166 volumetric images per BOLD run. Structural images were acquired using a T1-weighted, 3D magnetization-prepared rapid gradient-echo (MPRAGE) sequence [TR/TE/TI, 1500/2.83/800 ms; flip angle, 15°; voxel size (isotropic), 1 mm; FOV, 200 mm] with axial slices parallel to the Anterior Commissure (AC)-Posterior Commissure (PC) line. During each visit, subjects completed the following sequence of scans: (*i*) MPRAGE scan; (*ii*) one resting-state BOLD scan (not reported here), during which initial i.v. infusion occurred; and (*iii*) WM task acquisition across nine BOLD runs always following the initial resting-state scan. This sequence was performed during both saline and ketamine infusions.

fMRI Preprocessing. Preprocessing included: (*i*) slice-time correction; (*ii*) removal of the first 6 images from each run to reach steady state; (*iii*) elimination of odd/even slice intensity differences given interpolated acquisition; (*iv*) rigid body motion correction; (*v*) intensity normalization to a whole-brain mode value of 1,000 without bias or gain field correction; (*vi*) registration using a 12-parameter affine transform of the structural image to a template image in the Talairach coordinate system; (*vii*) coregistration of fMRI volumes to the structural image with 3-mm^3 resampling; and (*viii*) smoothing using a 6-mm full-width at half-maximum (FWHM) Gaussian kernel. All preprocessing results were inspected for movement and signal-to-noise (SNR) characteristics. Movement across BOLD runs never exceeded one functional voxel along any axis and no BOLD run had SNR of <100. Furthermore, there was no evidence of lower SNR for BOLD runs during ketamine vs. saline infusions (mean SNR ketamine, 279.03; mean SNR saline, 230.84). As done before (7), we calculated SNR after preprocessing but before atlas transformation (i.e., in each subject's native space) by obtaining the mean signal and SD for a given slice across the BOLD run, while excluding all nonbrain voxels across all frames. To further rule out possible effects of head motion on functional connectivity results (8), we have implemented an additional volume censoring (scrubbing) movement correction as reported by Power and colleagues (9, 10) (described comprehensively in *SI Text*, *tb-fcMRI, Preprocessing and analysis*).

fMRI Analyses. We used a general linear model (GLM) approach to estimate magnitudes of task-related activity for each voxel. We concatenated all of the BOLD runs across all three pretreatment sessions (i.e., 0, 50, and 180 mg) to estimate a "global" baseline across all three visits. Once concatenated, we estimated effects for 24 regressors: task condition (control vs. WM), infusion (ketamine vs. placebo), treatment (0, 50, 180 mg), and load (2 vs. 4 items). Treatment and load effects were modeled to ensure complete model specification, although reported effects did not interact with these factors. Given the focus on encoding, maintenance and probe phases of the task, we specifically isolated phase-specific activation using an assumed hemodynamic response function (HRF) GLM approach (11), as done in our prior work (12). To facilitate visual inspection, we also computed all activation and deactivation time courses using an unassumed HRF GLM approach across the first 24 frames of each trial (13) (see sections below for GLM details, second level analyses, symptom analyses, and task-based connectivity approach).

Second-level GLM analysis: WM effects. At the second level, we computed appropriate t tests and ANOVAs using the assumed GLM magnitudes for each trial component treating subjects as a random factor. All analyses were computed at the whole-brain level (i.e., voxel-wise) with the appropriate whole-brain type I error correction ascertained via AFNI's AlphaSim (14). AlphaSim considers voxel-wise and cluster-volume thresholds to establish a false-positive rate of 5%. Only regions corrected at $P < 0.05$ with a combined height and cluster level were considered to be significantly activated or deactivated in the whole-brain analysis. For coordinate reporting purposes, given the large number of active regions meeting a $P < 0.05$ correction in the whole-brain analyses, all identified maps were partitioned using a peak-splitting algorithm such that peaks were considered as separate if they were more than 10 mm apart (15, 16). Confirming the validity of our GLM approach, all of the results using the unassumed GLM analysis did not differ from the results obtained using an assumption-based model (13). All whole-brain analyses were visualized using Caret 5.5 software (http://brainvis.wustl.edu/wiki/index.php/Caret:Download) and projected onto the Population Average Landmark and Surface-based (PALS) atlas (17).

Second-level GLM analysis: ketamine effects. All reported second-level ketamine analyses followed a stringent and principled conjunction approach ensuring maximal specificity of task-relevant effects (see Fig. 1*B* for visual illustration). First, we identified areas, at each WM phase, showing a significant task condition (WM vs. control task contrast) effect. Second, we identified all regions exhibiting a significant infusion (ketamine vs. placebo) by task condition (WM vs. control) interaction. Next, we corrected these two maps at the appropriate whole-brain type-I error level and formed a conjunction (logical AND) of the two maps. This yielded a set of regions that were independently identified to be modulated by WM (first effect), as well as a modulation of WM by ketamine (second effect) (see Fig. S2 for resulting foci). This approach ensured that all surviving regions are modulated by task condition and that the task signal is modulated by ketamine.

Within-subject trial-to-trial relationship with accuracy. We also computed a second GLM for each subject that included an accuracy variable (correct vs. incorrect) as a covariate for each WM trial to enable examination of the within-subjects relationship between behavioral performance and brain activity, as done in our prior work (18). In other words, this allowed us to capture trial-to-trial variability in task response that was associated with correct vs. incorrect WM performance. As with all other analyses, the reported effects were computed using the assumed GLM estimates, but all visualized time courses were computed using an unassumed approach (13) (Fig. 5).

Across-subject symptom analyses. We investigated the relationship between the lack of DMN suppression and clinical symptom measures. Specifically, we averaged the signal across all DMN regions showing both a modulation by WM and by ketamine (i.e., surviving our conjunction approach) for each subject (given no a priori motivation to focus on any one region). Next, we computed the association between the obtained DMN values during WM specifically and standard clinical symptom measures obtained during an interview that took place immediately after the scan. We computed four correlations: (*i*) negative symptoms using the PANSS Negative Scale; (*ii*) positive symptoms using the PANSS Positive Scale; (*iii*) overall psychopathology as derived using the PANSS General Psychopathology Scale (6); and (*iv*) severity of dissociative symptoms using the sum of all items on the CADSS scale (5). To avoid false positives, we applied Bonferroni correction across these four analyses.

tb-fcMRI. ***Preprocessing and analysis.*** We further preprocessed the BOLD time series to remove sources of spurious variance that can drive between-region coupling: (*i*) high-pass filtering (>0.009 Hz) to remove low frequencies and scanner drift; and (*ii*) removal of motion correction parameters, ventricle, deep white matter, and global mean (GMS) signals, as well as their first derivatives using the GLM framework. We conducted all subsequent tb-fcMRI analyses on the residual values as done previously (18). We acknowledge that prior studies have shown that GMS removal can possibly induce some negative relationships (19). However, there is competing evidence showing that this preprocessing step is critical to optimize specificity of findings (20) and is widely used in the literature (21). Furthermore, this step was performed in an identical fashion across conditions; therefore, ketamine vs. placebo comparisons cannot be confounded by GMS removal. (*iii*) We implemented additional volume censoring (scrubbing) movement correction, as reported by Power and colleagues (9, 10), to ensure that head motion artifacts are not driving observed tb-fcMRI effects (8, 22). Briefly, image frames with possible artifactual fluctuations in intensity were identified using two criteria with a procedure suggested by Power et al. (10). First, frames in which sum of the displacement across all six rigid body movement correction parameters exceeded 0.5 mm (assuming a 50-mm cortical sphere radius) were identified. Second, root mean square (rms) of differences in intensity between the current and preceding frame was computed across all voxels and divided by mean intensity. Frames in which normalized rms exceeded the value of 3 were identified. The frames flagged by either criterion were marked for exclusion, as well as the one preceding and two frames following the flagged frame. Given that the average of two frames was used to compute per trial activity estimates for functional connectivity analysis (see below), trials that had either of the two frames marked for exclusion were omitted from the analyses. For completeness, we present effects both prior and after movement scrubbing (Fig. S7). In addition, we verified that the number of trials remaining after movement scrubbing did not differ across conditions, because one possibility is that movement scrubbing eliminated substantially more trials for the ketamine infusion. To this end, we computed an ANOVA with task condition (WM vs. control) × infusion (ketamine vs. placebo) as factors with the mean number of trials per subject as the dependent measure. There was no significant interaction [$F(1,18) = 0.65$; $P = 0.4$ (not significant)]. Moreover, the main effect of infusion [$F(1,18) = 4.94$; $P < 0.04$] was actually driven by there being a slightly higher fraction of frames removed from the placebo infusion. This effect is in the opposite direction to that expected by there being more movement-flagged trials for the ketamine infusion, indicating that the number of removed frames across infusions was not preferentially higher for ketamine.

Next, we computed the average BOLD signal value for the approximate delay period (time points 8 and 9) at each trial for each voxel in the image, as validated in our prior studies (18, 23). As noted, we averaged two time-points to reduce variability attributable to possible outlier frames. Next, we concatenated the values into 4D (brain volume × trial) time series that represented trial-to-trial variability. Extracting only specific time-locked components of the time series, as demonstrated in our prior work (7, 18, 23), ensured that the correlations are driven primarily by trial-to-trial variability and not overall task response. Furthermore, the issue of overall task response driving trial-to-trial variability is minimized given the slow event-related nature of the design.

Network definition and analysis. Our hypotheses focused on the relationship between the FP, cingulo-opercular (CO) control systems as defined by Dosenbach et al. (24), and the DMN as defined by Fox and colleagues (25) during the delay phase of WM. We included the CO system to examine specificity of the hypothesized FP-DMN relationship (all regions coordinates listed in Table S5). To control for individual anatomical variability, regions of interest (ROIs) were defined for each individual in two steps: (*i*) we created spherical ROIs (15 mm in diameter) in standard Talairach space centered on the reported coordinates for each region, as done previously (26); and (*ii*) we masked the resulting group ROIs with the individual subject-derived FreeSurfer (http://surfer.nmr.mgh.harvard.edu; version 4.1) segmentation of the high-resolution structural image that was previously registered to the standard Talairach space (27). This way, we excluded any voxels within the group-defined ROIs that did not represent the relevant gray matter for a given individual subject. We extracted the time series for each of these ROIs and computed the ROI-ROI correlation matrix across all ROIs for each participant for FP-DMN and CO-DMN pairs at the delay phase of the trial. All obtained correlations for each subject were converted to Fisher Z (Fz) values. Given no a priori motivation to focus on any one specific ROI-to-ROI connection, we averaged Fz values across all connections between the nodes of two networks of interest to produce a single "mean Fz" index of network connectivity [as done previously (18)]. Using this mean Fz index as the dependent measure, we computed a two-way repeated measures ANOVA with task condition (WM vs. control) × infusion (ketamine vs. placebo) as factors. All analyses are shown in Fig. S7. The FP-DMN results are also shown in Fig. 4.

Computational Modeling. To further relate observed BOLD effects to cellular-level hypothesized effects of ketamine, we constructed a parsimonious computational model of reciprocal interactions between task-activated and deactivated networks during WM. The current simulations are based on prior well-validated biophysically realistic models (28, 29), which are spiking local circuit models capable of WM and decision-making computations. The present model is comprised of two modules, one task-activated and one task-deactivated, each a local circuit of spiking excitatory (E) and inhibitory (I) cells. E cells interact with one another through horizontal connections mediating recurrent excitation via NMDA receptors (model scheme shown in Fig. 3*B*) and a pool of I cells that mediate feedback synaptic inhibition. We modeled the acute effects of ketamine as a reduction of NMDA conductance for both local and long-range E-I projections.

Model parameter details. Each module contains $N_E = 2{,}048$ pyramidal cells and $N_I = 512$ interneurons. The task-activated module is based on a well-validated model of spatial WM (28). We used the "modulated parameter set" of Compte et al. (28) with the modified E-E connectivity for increased WM robustness: $J_+ = 1.64$ (height of the Gaussian connectivity profile) and $\sigma_{E\text{-}E} = 14.4°$ (width of the Gaussian connectivity profile). The task-deactivated module contains a homogenous population of E cells and a population of I cells, with the following parameters changes from the modulated parameter set of Compte et al.: $J_+ = 1$ and $g_{E\text{-}E}$ is increased by 2% (i.e., recurrent excitatory conductance) to attain a uniform high firing-rate state. Excitatory projections between modules, mediated by NMDA receptors as in recurrent excitatory connections, are unstructured all-to-all, and target both E cells and I cells, to avoid assumptions about preferential anatomical connectivity patterns. Projection strengths from the task-activated module to the task-deactivated module are: $g_{E\text{-}E} = g_{E\text{-}I} = 200/N_E$ nS. Projection strengths from the task-deactivated module to the task-activated module are: $g_{E\text{-}E} = g_{E\text{-}I} = 60/N_E$ nS. These strengths were chosen to instantiate appropriate model behavior and patterns of both task-based activation and deactivation. Stimulus input is a current pulse to the E cells in the task-activated module with maximum of 200 nA and Gaussian profile width of 14.4°. Stimulus duration was 4.75 s for simulated BOLD traces as in the experiment (Fig. S3*B* and Fig. S5*C*), and 1 s for firing-rate traces (Figs. S4, S5*B*, and S6). Disinhibition by ketamine was implemented by a 1.25% reduction in the strength of all NMDA conductances onto I cells. Simulations were implemented with the Brian neural simulator (30); code is available from the authors upon request. Firing rate traces are calculated using a 50-ms exponential filter and averaged over 64 neurons (centered at the stimulus location for the task-activated module).

Interaction between modules. The interaction between task-activated and task-deactivated modules was modeled as follows: the task-activated module receives task-related sensory input and enables spatial WM through selective persistent firing. The task-deactivated module is characterized by high baseline firing rate at rest and deactivation at task onset, an effect shown across species (6, 31). The task-deactivated module does not have stimulus-selective cells and is only characterized as tonically active or deactivated. Long-range reciprocal projections between modules are from E cells and target both E cells and I cells, with the strengths biased onto I cells so that the net interaction between the modules is inhibitory, inducing anticorrelation in their activities (Fig. 3*B*). Strong stimulus input selectively excites a subset of E cells in the task-activated module. Activation of the task-activated module sends signals to the task-deactivated module that induce a deactivation attributable to biased projections onto I cells. In turn, deactivation of the task-deactivated module relieves the task-activated module of the inhibition by the task-deactivated module, which was present in the baseline state. These dynamics facilitate storage of the memorandum through persistent firing via reduction of excessive signals in the task-deactivated module. In this way, proper deactivation of the task-deactivated module supports successful WM performance (18).

Effects of ketamine. We modeled the acute effects of ketamine as a reduction of NMDA conductance for both local and long-range projections. There are the two sites for this reduction: onto I cells and onto E cells. By selectively reducing NMDA conductance onto one cell type, we explored preferential NMDA receptor antagonism on interneurons by ketamine (32, 33). Reduction of NMDA conductance onto I cells induces disinhibition of the local circuit by impairing the recruitment of feedback inhibition. As a result of disinhibition, the task-deactivated module's E cells have stronger reverberatory excitation and a higher baseline firing rate. Disinhibition, therefore, impedes suppression of the task-deactivated module by task onset. The task-deactivated module does not deactivate adequately and continues to exert inhibition on the task-activated module, impeding WM delay activity. As described in the main text, it is important to note that ketamine administration likely reduced NMDA conductance onto E cells as well (i.e., E-E conductance). However, exclusively modeling reduction in E-I conductance was sufficient to produce model behavior similar to our observed BOLD effects (Fig. S5). Furthermore, at achieved ketamine concentration (likely less than 50% occupancy), it is possible that ketamine more preferentially reduced conductance of NMDA receptors on inhibitory cells (32), which would be in line with present modeling results (Fig. S6). This computational model offers a hypothesis and a framework whereby disinhibition can lead to reduced task-related suppression in the task-deactivated module, as well as reduced WM signals in the task-activated module, leading to behavioral deficits.

Simulated BOLD signal. To further relate our modeling findings to observed BOLD results, we linked neuronal activity to neuronal ensemble activity to simulated BOLD response. To simulate an approximate BOLD signal in the model (shown in Fig. S5*C* and Fig. 3*B*), we followed a two-step approach validated in previous studies (34, 35): (*i*) simulate the local field potential (LFP) from synaptic activity in the network; and (*ii*) convolve the LFP signal with a hemodynamic response function, building on the correlation between LFP and BOLD signals (36). LFP is calculated as the absolute sum of all nonleak currents (AMPA, NMDA, GABA, and applied external) averaged across all pyramidal cells in a module (37). This model of LFP has been used successfully to link spiking circuit models to experimental LFP recordings (37). The BOLD signal was then calculated by convolving the LFP signal with a single γ distribution function of the form:

$$f(t) = \left(\frac{t-o}{d}\right)^{p-1}\left(\frac{\exp(-(t-o)/d)}{d(p-1)!}\right)^{p-1}$$

where timescale $d = 1.25$ s, delay $o = 2.25$ s, and shape parameter $p = 2$. We used this hemodynamic response function because it was also used to compute the assumed HRF for distinct task phases in the WM trail from the experimental data (38).

Local vs. long-range E-I conductance manipulation. Lastly, it is important to clarify a key insight the microcircuit model provides regarding the breakdown in task-based coordination between brain areas induced by ketamine. In the antagonistic architecture between modules, there are two mechanisms by which reduced E-I strength could potentially disrupt the proper pattern of activation and deactivation: (*i*) long-range (net inhibitory) connections between modules are weakened, impairing the ability of the task-activated module to shut down the task-deactivated module; and (*ii*) local disinhibition renders a hyperactive microcircuit less sensitive to the long-range input, so that the already high firing-task–deactivated module cannot be shut down even with an equal-strength, long-range suppressive input. A model implementation that does not instantiate biophysically realistic detail in each module would not suggest which mechanism plays the dominant role. We have carried out further simulations to isolate and test these two mechanisms. We found that local E/I balance is the crucial aspect of the model, suggesting a perspective on the importance of local circuit properties in controlling the nature of large-scale interactions between brain areas during cognitive tasks (Fig. S4).

1. First MB, Spitzer RL, Miriam G, Williams JBW (2002) *Structured Clinical Interview for DSM-IV-TR Axis I Disorders, Research Version, Non-Patient Edition (SCID-I/NP)* (Biometrics Research, New York State Psychiatric Institute, New York).
2. Patil ST, et al. (2007) Activation of mGlu2/3 receptors as a new approach to treat schizophrenia: A randomized Phase 2 clinical trial. *Nat Med* 13:1102–1107.
3. Corlett PR, et al. (2006) Frontal responses during learning predict vulnerability to the psychotogenic effects of ketamine: Linking cognition, brain activity, and psychosis. *Arch Gen Psychiatry* 63:611–621.
4. Domino SE, Domino LE, Domino EF (1982) Comparison of two and three compartment models of phencyclidine in man. *Subst Alcohol Actions Misuse* 3:205–211.
5. Bremner JD, et al. (1998) Measurement of dissociative states with the Clinician-Administered Dissociative States Scale (CADSS). *J Trauma Stress* 11:125–136.
6. Kay SR, Fiszbein A, Opler LA (1987) The positive and negative syndrome scale (PANSS) for schizophrenia. *Schizophr Bull* 13:261–276.
7. Anticevic A, Repovs G, Barch DM (2011) Emotion effects on attention, amygdala activation, and functional connectivity in schizophrenia. *Schizophr Bull*, 10.1093/schbul/sbq168.
8. Van Dijk KRA, Sabuncu MR, Buckner RL (2012) The influence of head motion on intrinsic functional connectivity MRI. *Neuroimage* 59:431–438.
9. Power JD, Barnes KA, Snyder AZ, Schlaggar BL, Petersen SE (2012) Spurious but systematic correlations in functional connectivity MRI networks arise from subject motion. *Neuroimage* 59:2142–2154.
10. Power JD, Barnes KA, Snyder AZ, Schlaggar BL, Petersen SE (2012) Steps toward optimizing motion artifact removal in functional connectivity MRI; A reply to Carp. *Neuroimage*.
11. Worsley KJ, Friston KJ (1995) Analysis of fMRI time-series revisited—again. *Neuroimage* 2:173–181.
12. Anticevic A, Repovs G, Barch DM (2011) Working memory encoding and maintenance deficits in schizophrenia: Neural evidence for activation and deactivation abnormalities. *Schizophr Bull*, 10.1093/schbul/sbr107.
13. Ollinger JM, Corbetta M, Shulman GL (2001) Separating processes within a trial in event-related functional MRI. *Neuroimage* 13:218–229.
14. Cox RW (1996) AFNI: Software for analysis and visualization of functional magnetic resonance neuroimages. *Comput Biomed Res* 29:162–173.
15. Michelon P, Snyder AZ, Buckner RL, McAvoy M, Zacks JM (2003) Neural correlates of incongruous visual information. An event-related fMRI study. *Neuroimage* 19:1612–1626.
16. Kerr DL, Gusnard DA, Snyder AZ, Raichle ME (2004) Effect of practice on reading performance and brain function. *Neuroreport* 15:607–610.
17. Van Essen DC (2005) A Population-Average, Landmark- and Surface-based (PALS) atlas of human cerebral cortex. *Neuroimage* 28:635–662.
18. Anticevic A, Repovs G, Shulman GL, Barch DM (2010) When less is more: TPJ and default network deactivation during encoding predicts working memory performance. *Neuroimage* 49:2638–2648.
19. Murphy K, Birn RM, Handwerker DA, Jones TB, Bandettini PA (2009) The impact of global signal regression on resting state correlations: Are anti-correlated networks introduced? *Neuroimage* 44:893–905.
20. Fox MD, Zhang D, Snyder AZ, Raichle ME (2009) The global signal and observed anticorrelated resting state brain networks. *J Neurophysiol* 101:3270–3283.
21. Biswal BB, et al. (2010) Toward discovery science of human brain function. *Proc Natl Acad Sci USA* 107:4734–4739.
22. Satterthwaite TD, et al. (2012) Impact of in-scanner head motion on multiple measures of functional connectivity: Relevance for studies of neurodevelopment in youth. *Neuroimage* 60:623–632.
23. Anticevic A, Repovs G, Barch DM (2010) Resisting emotional interference: Brain regions facilitating working memory performance during negative distraction. *Cogn Affect Behav Neurosci* 10:159–173.
24. Dosenbach NU, et al. (2007) Distinct brain networks for adaptive and stable task control in humans. *Proc Natl Acad Sci USA* 104:11073–11078.
25. Fox MD, et al. (2005) The human brain is intrinsically organized into dynamic, anticorrelated functional networks. *Proc Natl Acad Sci USA* 102:9673–9678.
26. Repovs G, Csernansky JG, Barch DM (2011) Brain network connectivity in individuals with schizophrenia and their siblings. *Biol Psychiatry* 69:967–973.
27. Talairach J, Tournoux P (1988) *Co-planar Stereotaxic Atlas of the Human Brain* (Thieme, New York).
28. Compte A, Brunel N, Goldman-Rakic PS, Wang XJ (2000) Synaptic mechanisms and network dynamics underlying spatial working memory in a cortical network model. *Cereb Cortex* 10:910–923.
29. Wang XJ (2002) Probabilistic decision making by slow reverberation in cortical circuits. *Neuron* 36:955–968.
30. Goodman DF, Brette R (2009) The brian simulator. *Front Neurosci* 3:192–197.
31. Shulman GL, et al. (1997) Common blood flow changes across visual tasks: I. Increases in subcortical structures and cerebellum but not in nonvisual cortex. *J Cogn Neurosci* 9:624–647.
32. Kotermanski SE, Johnson JW (2009) Mg2+ imparts NMDA receptor subtype selectivity to the Alzheimer's drug memantine. *J Neurosci* 29:2774–2779.
33. Krystal JH, et al. (2003) NMDA receptor antagonist effects, cortical glutamatergic function, and schizophrenia: Toward a paradigm shift in medication development. *Psychopharmacology (Berl)* 169:215–233.
34. Deco G, Rolls ET, Horwitz B (2004) "What" and "where" in visual working memory: A computational neurodynamical perspective for integrating FMRI and single-neuron data. *J Cogn Neurosci* 16:683–701.
35. Stemme A, Deco G, Busch A, Schneider WX (2005) Neurons and the synaptic basis of the fMRI signal associated with cognitive flexibility. *Neuroimage* 26:454–470.
36. Logothetis NK, Pauls J, Augath M, Trinath T, Oeltermann A (2001) Neurophysiological investigation of the basis of the fMRI signal. *Nature* 412:150–157.
37. Mazzoni A, Panzeri S, Logothetis NK, Brunel N (2008) Encoding of naturalistic stimuli by local field potential spectra in networks of excitatory and inhibitory neurons. *PLOS Comput Biol* 4:e1000239.
38. Boynton GM, Engel SA, Glover GH, Heeger DJ (1996) Linear systems analysis of functional magnetic resonance imaging in human V1. *J Neurosci* 16:4207–4221.

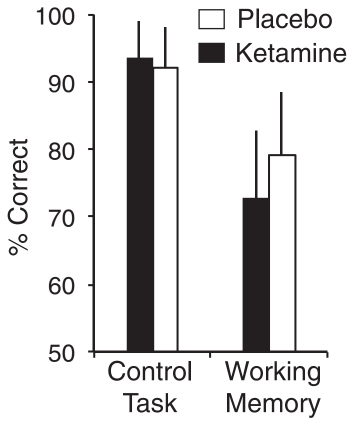

Fig. S1. Behavioral results. Accuracy (% correct) is shown across both control and WM tasks following placebo (white bars) and ketamine infusions (black bars). Error bars reflect ±1 SEM.

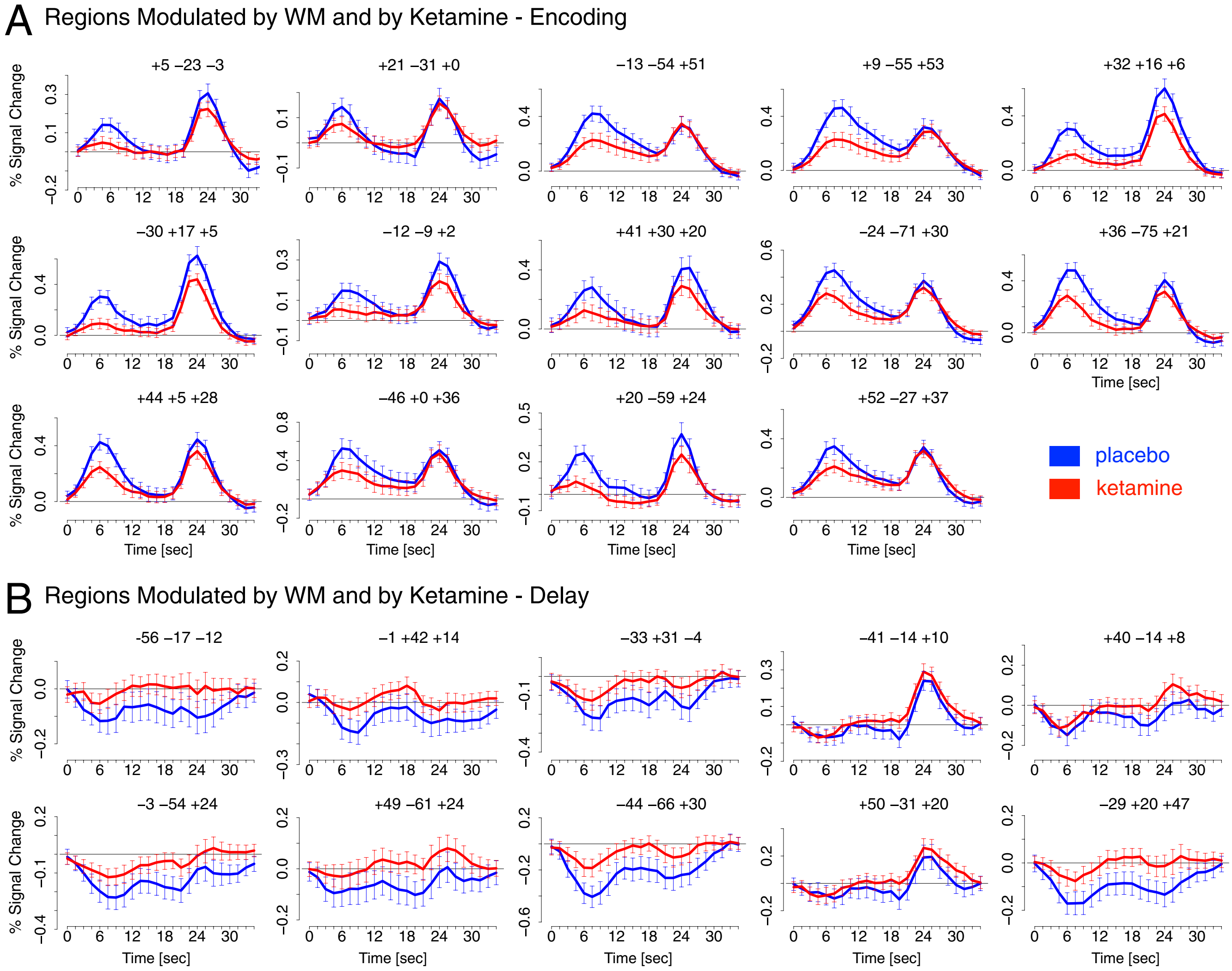

Fig. S2. Regions showing effects of WM and modulation by ketamine. All of the shown regions survived the stringent conjunction approach [i.e., both main effect of task condition (WM vs. control) and a task condition × infusion (ketamine vs. placebo) interaction]. Reconstructed time courses are displayed for regions showing effects at encoding (*A*) and delay (*B*) phases of the trial. All effects were isolated using an assumed HRF but visualized using an unassumed HRF analysis to allow inspection of time courses across the entire trial. As noted in the main text, no regions at the probe phase survived the conjunction. *x*, *y*, and *z* coordinates above each figure are represented in Talairach stereotaxic space. Coordinates for all regions are also listed in Table S4.

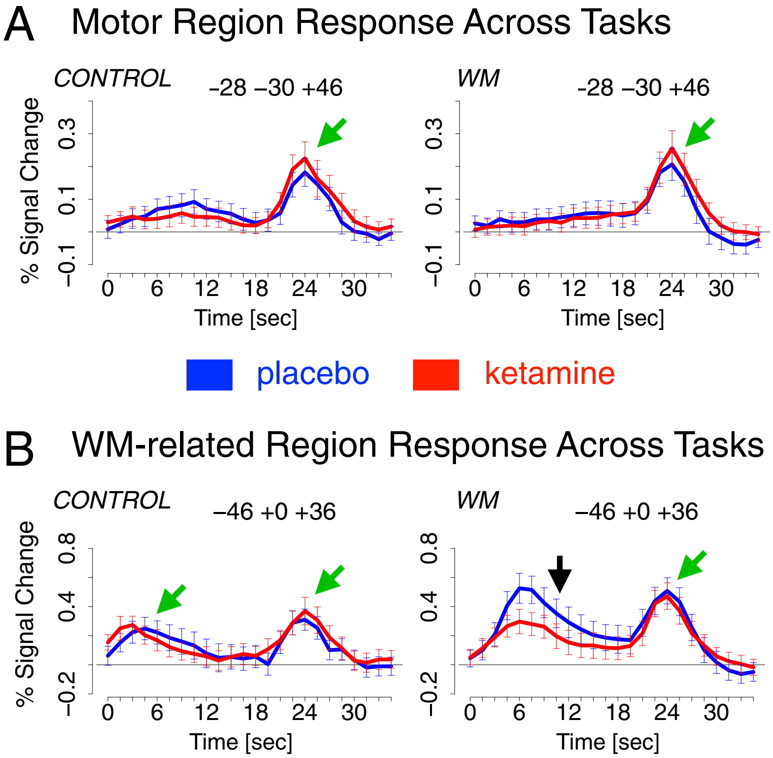

Fig. S3. Illustrating preferential ketamine effects across regions and tasks. (*A*) Motor cortex region (proximal to BA 4) response is shown for the control task (*Left*) and WM task (*Right*). As highlighted by green arrows, the BOLD response across both task conditions at the probe phase, where a motor response is required, is not attenuated by ketamine (in fact it is numerically higher). Note: we plotted the left motor cortex response given that all subjects were right-handed. (*B*) We also highlight preferential ketamine effects on WM encoding/delay signal in a region activated by the WM task. (*Left*) No difference is found between ketamine and placebo response during the control task early in the trial and during the probe phase, highlighted with green arrows. (*Right*) Attenuation of BOLD signal is shown for ketamine relative to placebo during WM encoding/delay phases of the trial (black arrow) but, again, no difference at the probe phase. Together, these results are inconsistent with the possibility that ketamine administration compromised BOLD responses in general but suggest a more preferential disruption of computations critical for WM-related processing.

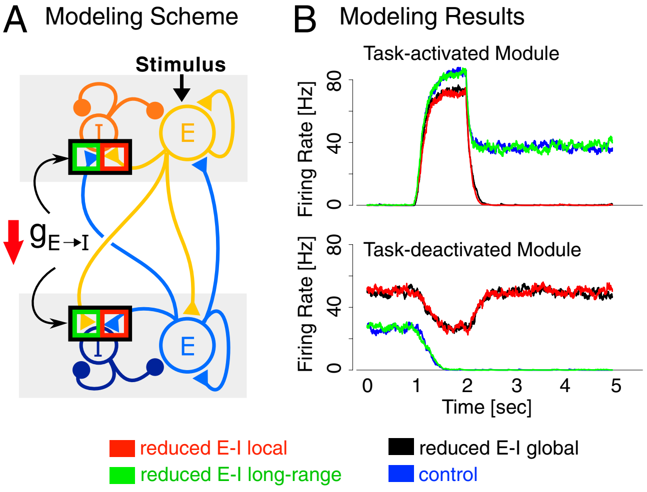

Fig. S4. Effects of reducing local vs. long-range E-I synapses. (*A*) Model scheme illustrating effects of a small reduction in NMDA conductance at local microcircuit E-I synapses (red box) vs. long-range between-module E-I synapses (green box), as well as global reduction in E-I synapses (black box surrounding the smaller boxes). (*B*) Modeling results illustrating reduction in NMDA conductance for global (black), long-range (green), and local microcircuit (red) E-I synapses. In the global case, all NMDA conductances onto interneurons were reduced by 1.25%, as in the main text. For both local and long-range cases, this strength of reduction was the same value (i.e., 1.25%). The local reduction regime produces similar model behavior dynamics as observed in the global reduction regime. In contrast, the long-range reduction regime produces similar model behavior dynamics as observed in the control regime. Therefore, the observed disruption to model performance is not primarily driven by reduced inhibitory coupling between modules but instead driven primarily by local microcircuit disinhibition. That is, under local disinhibition, the already high-firing, task-deactivated module cannot be shut down even though long-range connections are unaffected.

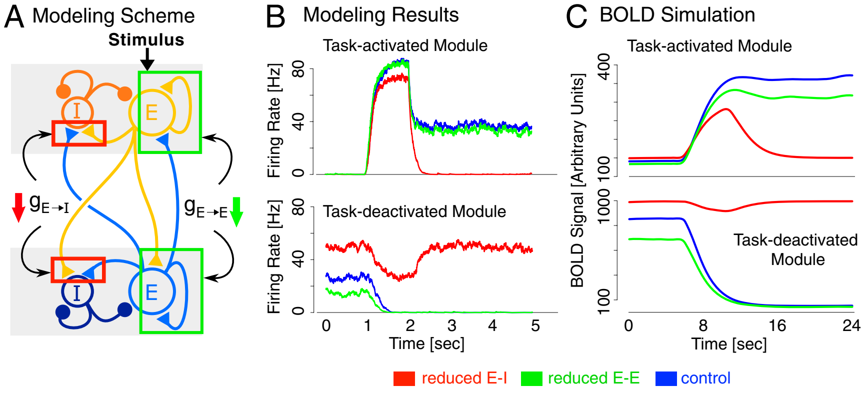

Fig. S5. Effects of reducing E-I vs. E-E synapses and simulated BOLD signal. (*A*) Model scheme illustrating effects of a small reduction in NMDA conductance at E-E synapses (green box) vs. E-I synapses (red box). (*B*) Modeling results illustrating reduction in NMDA conductance for E-E (green) vs. E-I synapses (red). The E-E manipulation facilitates deactivation of the task-deactivated module, contrary to the experimental results presented in the main text. (*C*) We juxtapose the predicted BOLD signal (also shown in the main text; Fig. 3*B*) with the model-generated firing rate traces. As noted, the BOLD signal is derived from the simulated LFP on the time scale comparable to a single WM trial in the experiment. Differences between the simulated and experimental BOLD traces highlighted in the main text likely reflect contributions from multiple cell types that are not instantiated in the model. That is, the model contains only two subtypes of cells that are involved in generating persistent WM-related activity. Nevertheless, the simulated BOLD signal still qualitatively captured the observed task-dependent activation/deactivation that was observed experimentally. For comparison with experimental results, the stimulus duration in *C* was extended to 4.75 s, as in the experiment. The WM delay was simulated over 16 s as done experimentally. Notes: for reduced E-E conductance case, all NMDA conductances onto pyramidal cells were reduced by 0.5%; for reduced E-I conductance case, all NMDA conductances onto interneurons were reduced by 1.25%. See Fig. S6 for systematic characterization of model dependence on these two parameters. The different magnitudes of BOLD signal deflection across modules are attributable to the different proportions of neurons with a significant activity change (i.e., for the task-activated module only a fraction of preferentially-stimulated cells increase their firing rate and contribute to the LFP).

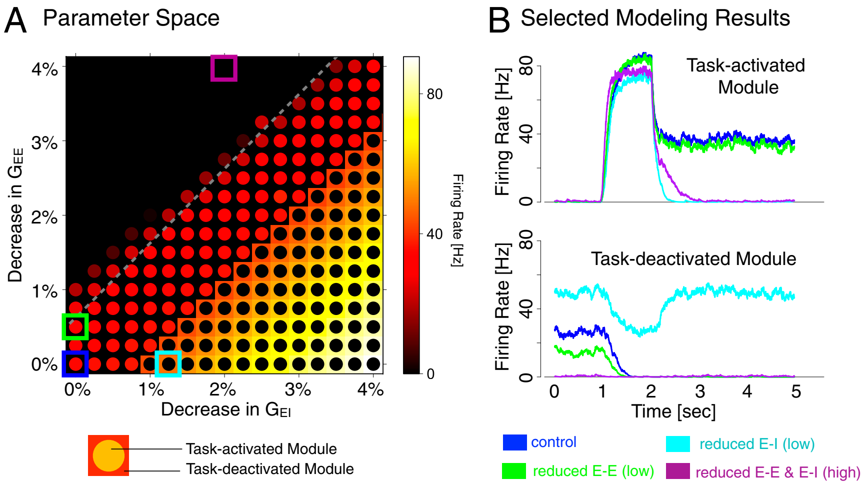

Fig. S6. Parameter space illustrating dependence of model regimes on parameter selection. (*A*) Dependence of the modules' delay-period firing rates on reductions to NMDA conductance onto interneurons ($G_{E\text{-}I}$) and onto pyramidal cells ($G_{E\text{-}E}$). There are generally three observed regimes in this parameter space: (*i*) along the middle diagonal (approximately equal reduction in E-I and E-E conductances), E/I balance is roughly maintained and the model functions properly during the WM delay, with the task-activated module preserved at high firing rate and the task-deactivated module at low firing rate. (*ii*) In the lower right portion of the parameter space (preferential reduction of E-I conductance), disinhibition disrupts model function, so that during the delay the task-deactivated module is still at high firing rate and the task-activated module exhibits low firing rate and fails to sustain WM representation. (*iii*) In the upper left portion of the parameter space (preferential reduction of E-E conductance), both modules exhibit low firing rates during the delay. This is because with the low E/I ratio neither module has sufficient recurrent excitation to sustain a high-firing state. The dashed gray line marks the minimum E/I ratio necessary for the task-deactivated module to sustain a uniform high-firing state before stimulus onset (i.e., before deactivation). Below the line, the module supports a high-firing state before stimulus onset. Above the line, there is insufficient recurrent excitation to support the high-firing state. Therefore, before stimulus onset, both modules are in low-firing states. (*B*) Model traces corresponding to four selected points from the parameters space: control condition (blue); disinhibition via subtle E-I reduction (cyan) as shown in the main text; subtle E-E reduction (green); and hypothesized higher level of ketamine, which may result in higher E-E and E-I reduction (purple). These selected parameters illustrate that with a subtle E-E reduction (green) model results did not match observed experimental effect in that the task-deactivated module is still successfully suppressed in the model. In contrast, at higher levels of both E-E and E-I reduction (purple), there was a collapse of high-rate states across both modules (as may be expected in anesthesia). Both of these sets of regimes were less consistent with our experimental effects. The visualization method for complex multi-parameter space in *A* was provided by Dr. Eve Marder and Gabrielle Gutierrez (1).

1. Gutierrez GJ (2012) Dynamics of multi-functional, pattern-generating neuronal networks. PhD thesis (Brandeis University, Waltham, MA).

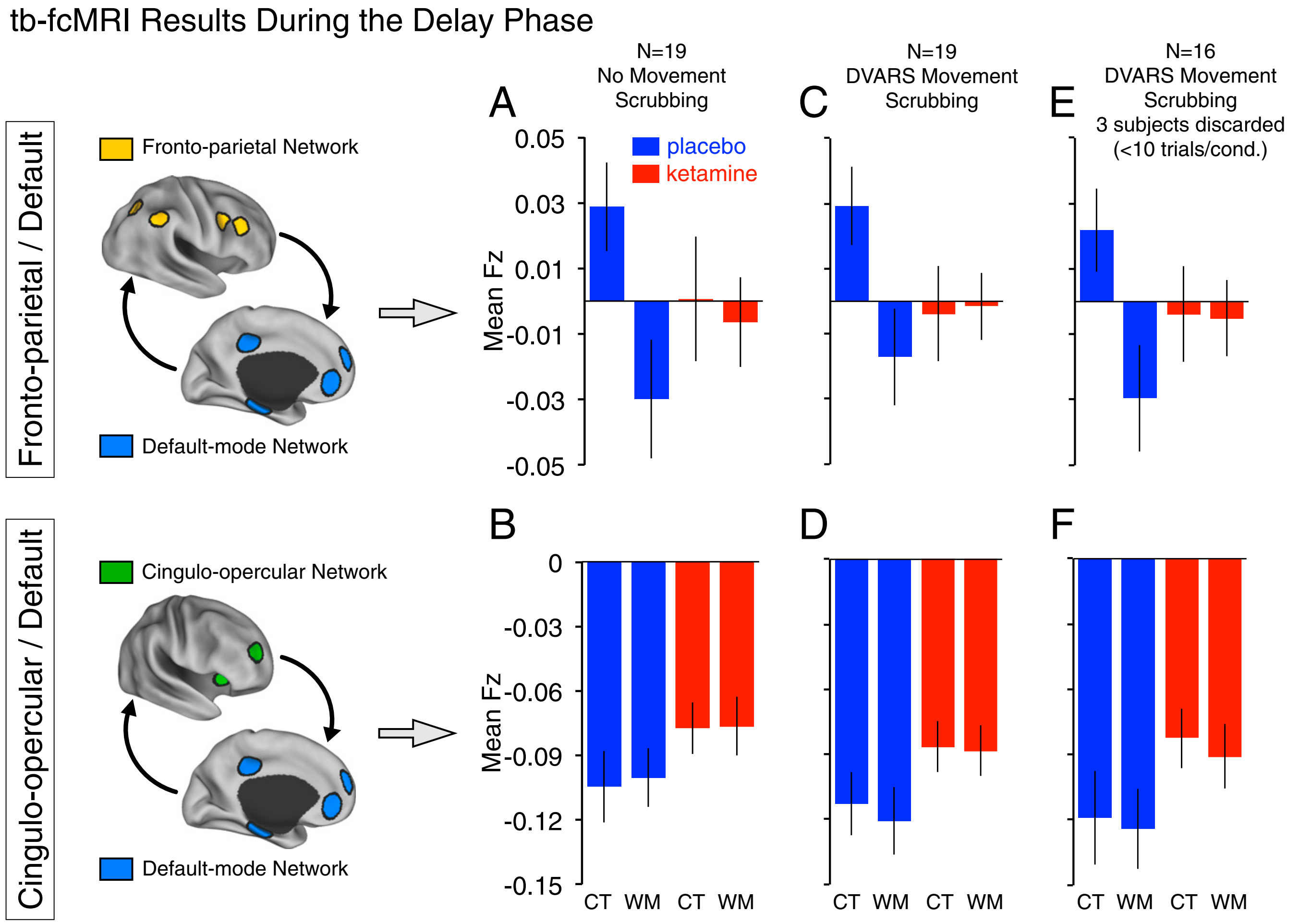

Fig. S7. Effects of ketamine on tb-fcMRI findings and effects of movement. We illustrate the effects of ketamine (red) vs. placebo (blue) on tb-fcMRI for the FP and default mode network (DMN) (upper graphs), as well as for the cingulo-opercular (CO): DMN network relationships (lower graphs) during the delay phase of WM. We show the pattern of results across the two network analyses without additional volume censoring (scrubbing) movement correction implemented (*A* and *B*), after movement scrubbing (1, 2) (*C* and *D*), and after additionally removing three subjects for whom movement scrubbing removed a somewhat larger number of trials, resulting in <10 useable trials for any one condition (*E* and *F*). As evidenced across all analyses, there was a significant task condition (control vs. WM) × infusion (ketamine vs. placebo) interaction for the DMN-FP networks during the delay phase [$F(1,18) = 11.09$; $P < 0.004$], which remained significant even after movement scrubbing [$F(1,18) = 6.1$; $P < 0.025$] and after removal of three additional subjects that had <10 trials left for any given condition after movement scrubbing was implemented [$F(1,15) = 5.13$; $P = 0.038$]. The effect of ketamine on WM trials was preferential to the FP-DMN network, because there was no task condition (control vs. WM) × infusion (ketamine vs. placebo) interaction across the CO-DMN comparisons (but there was a main effect of infusion for the CO-DMN tb-fcMRI). Error bars reflect ±1 SEM.

1. Power JD, Barnes KA, Snyder AZ, Schlaggar BL, Petersen SE (2012) Spurious but systematic correlations in functional connectivity MRI networks arise from subject motion. *Neuroimage* 59:2142–2154.
2. Power JD, Barnes KA, Snyder AZ, Schlaggar BL, Petersen SE (2012) Steps toward optimizing motion artifact removal in functional connectivity MRI; a reply to Carp. *Neuroimage*, 10.1016/j.neuroimage.2012.03.017.

Table S1. Regions showing significant WM effects during the encoding phase

x	*y*	*z*	Hemisphere	Anatomical landmark	Peak *Z* statistic	Size (mm^3)
Task-positive						
20	−2	61	Right	Middle frontal gyrus (BA 6)	6.02	10,746
−15	−64	45	Left	Precuneus (BA 7)	5.74	10,692
19	−67	53	Right	Precuneus (BA 7)	5.60	11,772
−30	−8	51	Left	Precentral gyrus (BA 6)	5.53	7,722
41	−61	36	Right	Inferior parietal cortex (BA 39)	5.44	8,748
29	−74	13	Right	Middle occipital gyrus	5.41	5,184
−32	−48	48	Left	Inferior parietal cortex (BA 40)	5.17	5,724
35	−48	50	Right	Inferior parietal cortex (BA 40)	5.17	8,775
−29	−81	23	Left	Middle occipital gyrus	5.04	8,802
50	−23	38	Right	Postcentral gyrus (BA 2)	4.90	5,157
41	5	27	Right	Precentral gyrus (BA 6/9)	4.83	7,776
−30	18	9	Left	Insular cortex (BA 13)	4.62	2,133
−42	−37	31	Left	Parietal cortex (BA 40)	4.60	3,213
32	16	8	Right	Insular cortex (BA 13)	4.50	2,808
51	−58	−6	Right	Middle occipital gyrus	4.31	3,915
−5	0	51	Left	Medial frontal gyrus (BA 6)	4.26	6,426
−30	−60	−27	Left	Cerebellum/culmen	4.08	3,159
−46	0	30	Left	Precentral gyrus (BA 6)	3.99	3,861
−46	−64	−5	Left	Middle occipital gyrus	3.94	3,456
1	−32	−13	Right	Brainstem/midbrain	3.73	2,538
−49	−17	46	Left	Postcentral gyrus (BA 2/3)	3.72	3,429
−14	−10	1	Left	Thalamus	3.60	1,134
−36	−38	−35	Left	Cerebellum	3.55	1,485
13	−12	−2	Right	Thalamus	3.19	1,485
43	37	21	Right	Middle frontal gyrus (BA 46)	3.01	1,485
Task-negative						
38	−21	15	Right	Transverse temporal gyrus (BA 41)	−4.92	9693
−5	−57	27	Left	Posterior cingulate gyrus (BA 31)	−4.83	11988
−57	−14	14	Left	Transverse temporal gyrus (BA 41)	−4.58	7560
−45	−64	35	Left	Angular gyrus (BA 39)	−4.56	9261
58	−30	10	Right	Superior temporal gyrus (BA 41)	−4.55	10287
−46	−35	9	Left	Superior temporal gyrus (BA 41)	−4.50	10314
−50	20	14	Left	Inferior frontal gyrus (BA 44/45)	−4.39	3996
−36	−9	7	Left	Insula	−4.38	6642
17	35	47	Right	Superior frontal gyrus (BA 8)	−4.37	2160
60	−6	17	Right	Postcentral gyrus (BA 43)	−4.37	7209
−37	43	1	Left	Inferior frontal gyrus (BA 10)	−4.26	5859
−13	53	30	Left	Superior frontal gyrus (BA 8/9)	−4.23	5643
−35	18	48	Left	Superior frontal gyrus (BA 8)	−4.20	6,993
30	−81	−30	Right	Cerebellum	−4.15	4,023
−60	−50	30	Left	Supramarginal gyrus	−4.14	2,673
−11	29	51	Left	Superior frontal gyrus (BA 8)	−4.10	8,289
−45	2	−8	Left	Superior temporal gyrus (BA 22)	−4.09	1,971
56	−27	−11	Right	Middle temporal gyrus (BA 21)	−3.99	5,103
15	60	21	Right	Superior frontal gyrus (BA 10)	−3.91	3,969
60	−52	28	Right	Supramarginal gyrus	−3.86	3,483
−22	−87	−30	Left	Cerebellum	−3.86	2,268
−55	−28	−13	Left	Middle temporal gyrus (BA 21)	−3.84	4,860
11	−90	−29	Right	Cerebellum	−3.77	2,025
−25	−63	10	Left	Posterior cingulate gyrus (BA 30)	−3.72	3,699
3	−84	33	Right	Occipital lobe/cuneus (BA 19)	−3.62	4,455
−39	25	−8	Left	Inferior frontal gyrus (BA 47)	−3.60	3,483
−16	−46	2	Left	Parahippocampal gyrus	−3.52	2,781
−38	−79	−42	Left	Cerebellum	−3.50	702
23	−51	21	Right	Parietal lobe	−3.48	3,861
1	35	−16	Right	Medial frontal gyrus (BA 11)	−3.43	2,295
49	28	2	Right	Inferior frontal gyrus (BA 47)	−3.35	2,160
16	−57	−13	Right	Posterior cingulate gyrus (BA 30)	−3.33	4,104
−4	51	12	Left	Medial frontal gyrus (BA 10)	−3.27	1,755
−11	−33	38	Left	Cingulate gyrus (BA 31)	−3.27	1,809
63	−8	−15	Right	Middle temporal gyrus (BA 21)	−3.19	783
−13	−57	−15	Left	Cerebellum	−3.16	1,431
22	−33	−2	Right	Parahippocampal gyrus	−3.06	972
48	−65	−36	Right	Cerebellum	−2.98	864

Table S2. Regions showing significant WM effects during the delay phase

x	*y*	*z*	Hemisphere	Anatomical landmark	Peak *Z* statistic	Size (mm^3)
Task-positive						
−13	−56	56	Left	Superior parietal cortex (BA 7)	4.86	9,774
21	−60	55	Right	Superior parietal cortex (BA 7)	4.76	13,014
36	−9	53	Right	Precentral gyrus (BA 6)	4.43	11,178
25	−45	31	Right	Parietal cortex (BA 31)	4.40	7,452
5	−50	67	Right	Postcentral gyrus (BA 5/7)	4.25	2,808
41	−70	16	Right	Middle temporal gyrus (BA 37)	4.22	5,967
−17	10	−20	Left	Inferior frontal gyrus (BA 47)	4.22	1,782
−15	−22	−30	Left	Brainstem	4.19	4,644
18	−2	−24	Right	Uncus/parahippocampal gyrus	4.16	4,077
28	−80	39	Right	Parietal cortex (BA 19)	4.16	5,940
29	−24	−28	Right	Parahippocampal gyrus	4.15	1,944
39	−34	43	Right	Inferior parietal cortex (BA 40)	4.14	11,853
−35	−49	45	Left	Inferior parietal cortex (BA 40)	4.14	9,693
−43	−61	−2	Left	Middle temporal gyrus (BA 37)	4.06	4,374
−27	−8	47	Left	Middle frontal gyrus (BA 6)	4.01	7,641
60	−50	−19	Right	Temporal cortex (BA 37)	4.00	3,267
−14	−45	−24	Left	Cerebellum	3.96	5,940
−28	−46	27	Left	Parietal lobe/subgyral	3.96	3,645
46	−57	−4	Right	Middle temporal gyrus (BA 37)	3.91	8,694
49	2	30	Right	Precentral gyrus (BA 6)	3.91	5,751
24	−8	29	Right	Subgyral white matter	3.90	8,937
18	−31	15	Right	Thalamus/pulvinar	3.80	3,564
15	−56	−26	Right	Cerebellum	3.78	3,186
−50	−20	−32	Left	Inferior temporal gyrus (BA 20)	3.75	1,836
40	43	27	Right	Superior frontal gyrus (BA 9)	3.70	2,457
8	−29	−23	Right	Brainstem/midbrain	3.68	4,050
−39	−50	−37	Left	Cerebellum	3.65	6,048
−24	−95	4	Left	Middle occipital gyrus (BA 18)	3.54	3,456
0	−30	61	Midline	Medial frontal gyrus (BA 6)	3.48	3,564
−2	−69	−30	Left	Cerebellum	3.39	2,781
27	19	10	Right	Insular cortex (BA 13)	3.35	1,890
−32	−26	−12	Left	Parahippocampal gyrus	3.27	2,079
33	−29	62	Right	Precentral gyrus (BA 4)	3.26	2,241
35	−48	−33	Right	Cerebellum	3.18	1,431
−55	−44	−11	Left	Middle temporal gyrus (BA 20/37)	3.18	2,052
−21	−26	17	Left	Thalamus/pulvinar	3.16	2,214
−6	5	51	Midline	Medial frontal gyrus (BA 6)	3.04	1,080
Task-negative						
−7	−57	30	Midline	Parietal cortex (BA 7)	−4.79	10,341
−21	38	2	Left	Anterior cingulate (BA 32)	−4.55	4,185
2	28	1	Midline	Anterior cingulate (BA 24)	−4.19	10,260
−45	−69	36	Left	Angular gyrus (BA 39)	−4.16	7,533
61	−55	16	Right	Superior temporal gyrus (BA 22)	−4.15	2,214
−3	−56	8	Midline	Posterior cingulate (BA 30)	−4.15	5,184
11	45	13	Right	Medial frontal gyrus (BA 10)	−4.14	4,185
31	−94	6	Right	Middle occipital gyrus (BA 18)	−4.13	2,970
49	−65	40	Right	Inferior parietal cortex (BA 39)	−4.07	4,995
−24	−80	33	Left	Precuneus (BA 7)	−4.07	7,587
−55	−23	52	Left	Postcentral gyrus (BA 1/2)	−4.06	1,701
−7	49	22	Midline	Posterior cingulate (BA 30)	−3.90	11,988
34	−21	5	Right	Putamen	−3.89	6,723
−60	−52	40	Left	Inferior parietal cortex (BA 40)	−3.88	1,539
−37	14	51	Left	Middle frontal gyrus (BA 6)	−3.81	3,780
−43	−11	16	Left	Insular cortex (BA 13)	−3.69	6,399
57	−28	17	Right	Superior temporal gyrus (BA 42)	−3.69	2,025
16	−95	24	Right	Occipital lobe (BA 19)	−3.61	1,080
−57	−17	−10	Left	Middle temporal gyrus (BA 21)	−3.54	1,593
−15	24	57	Left	Superior frontal gyrus (BA 6)	−3.45	4,158
52	−13	−22	Right	Fusiform gyrus	−3.35	2,052
−1	39	50	Midlinel	Superior frontal gyrus (BA 8)	−3.27	3,672
35	−76	−31	Left	Cerebellum	−3.21	1,026

Table S3. Regions showing significant WM effects during the probe phase

x	*y*	*z*	Hemisphere	Anatomical landmark	Peak *Z* statistic	Size (mm^3)
Task-positive						
33	17	2	Right	Insular cortex (BA 13)	5.14	7,344
−31	17	1	Left	Insular cortex (BA 13)	5.02	5,940
43	17	34	Right	Middle frontal gyrus (BA 9)	4.22	5,157
−1	16	50	Midline	Superior frontal gyrus (BA 6)	4.21	9,261
3	32	20	Midline	Anterior cingulate (BA 32)	4.11	7,209
41	−46	45	Right	Parietal cortex (BA 40)	3.84	4,509
17	−60	23	Right	Temporal lobe (BA 31)	3.84	1,593
41	−70	40	Right	Parietal lobe/precuneus	3.75	2,322
−41	21	26	Left	Middle frontal gyrus (BA 9)	3.73	1,485
−40	−48	40	Left	Parietal cortex (BA 40)	3.60	4,050
−43	1	33	Left	Precentral gyrus (BA 6)	3.55	2,295
−28	−4	49	Left	Middle frontal gyrus (BA 6)	3.47	1,215
10	−69	49	Right	Superior parietal lobe (BA 7)	3.42	2,889
27	−2	57	Right	Middle frontal gyrus (BA 6)	3.41	3,024
7	−26	23	Midline	Cingulate gyrus (BA 23)	3.16	1,269
−13	−69	46	Left	Precuneus (BA 7)	3.11	1,971
3	−18	−9	Midline	Brainstem/midbrain	2.88	1,026
Task-negative						
−17	40	46	Left	Superior frontal gyrus (BA 8)	−4.96	7,938
13	−88	36	Right	Occipital lobe/cuneus	−4.69	2,241
60	−37	17	Right	Superior temporal gyrus (BA 22)	−4.26	1,917
20	−94	17	Right	Middle occipital gyrus (BA 18/19)	−4.24	4,374
0	32	−9	Midline	Anterior cingulate (BA 32)	−4.15	2,997
15	−24	59	Right	Precentral gyrus (BA 4)	−4.15	4,212
16	39	50	Right	Superior frontal gyrus (BA 8)	−4.06	1,701
40	−87	−2	Right	Inferior occipital gyrus (BA 18)	−4.05	1,539
−35	21	52	Left	Superior frontal gyrus (BA 8)	−4.05	3,024
−27	−32	−13	Left	Parahippocampal gyrus	−4.04	1,782
−53	−13	−15	Left	Middle temporal gyrus (BA 21)	−4.04	4,401
−10	−24	62	Left	Medial frontal gyrus (BA 6)	−4.01	2,700
−40	−71	41	Left	Parietal lobe/precuneus	−3.97	1,755
−6	−56	22	Midline	Posterior cingulate (BA 31)	−3.91	4,077
−30	−10	−23	Left	Parahippocampal gyrus	−3.86	6,048
35	−10	17	Right	Insular cortex (BA 13)	−3.78	2,322
−6	50	1	Midline	Medial frontal gyrus (BA 10/32)	−3.76	5,778
−40	−29	22	Left	Insular cortex	−3.67	1,404
39	−25	4	Right	Superior temporal gyrus	−3.66	1,404
24	−10	−17	Right	Parahippocampal gyrus/amygdala	−3.63	2,457
−12	56	25	Left	Superior frontal gyrus (BA 9/10)	−3.52	3,240
55	−12	22	Right	Postcentral gyrus (BA 4/43)	−3.43	3,213
52	−11	−6	Right	Middle temporal gyrus (BA 22)	−3.26	2,646
39	−26	54	Right	Postcentral gyrus (BA 3)	−3.21	2,592
33	−34	24	Right	Insular cortex	−3.17	1,080
−36	16	−30	Left	Superior temporal gyrus (BA 38)	−3.13	1,188
52	−68	7	Right	Middle temporal gyrus (BA 37/39)	−3.05	1,134
49	−8	45	Right	Precentral gyrus (BA 4)	−3.05	1,107
−62	−25	5	Left	Superior temporal gyrus (BA 22)	−3.03	837
−56	−67	27	Left	Middle temporal gyrus (BA 39)	−2.93	891

Table S4. Regions showing both a significant effect of WM, as well as a modulation by ketamine

x	*y*	*z*	Hemisphere	Anatomical landmark	Size (mm^3)
Encoding: task- positive					
5	−23	−3	Right	Brainstem/midbrain	3,672
21	−31	0	Right	Thalamus	729
−13	−54	51	Left	Superior parietal cortex (BA 7)	1,701
9	−55	53	Right	Superior parietal cortex (BA 7)	999
32	16	6	Right	Insular cortex (BA 13)	2,187
−30	17	5	Left	Insular cortex (BA 13)	1,080
−12	−9	2	Left	Thalamus	756
41	30	20	Right	Middle frontal gyrus (BA 46)	783
−24	−71	30	Left	Parietal cortex (BA 19)	4,077
36	−75	21	Right	Parietal cortex (BA 19)	1,485
44	5	28	Right	Precentral gyrus (BA 9/46)	5,130
−46	0	36	Left	Precentral gyrus (BA 9/46)	891
20	−59	24	Right	Precuneus	378
52	−27	37	Right	Postcentral gyrus (BA 2/40)	729
Maintenance: task-negative					
−56	−17	−12	Left	Middle temporal gyrus (BA 21)	1,053
−1	42	14	Midline	Medial frontal gyrus (BA 32)	20,385
−33	31	−4	Left	Inferior frontal gyrus (BA 47)	621
−41	−14	10	Left	Superior temporal lobe (BA 13)	3,564
40	−14	8	Right	Superior temporal lobe (BA 13)	648
−3	−54	24	Midline	Posterior cingulate (BA 31)	12,852
49	−61	24	Right	Superior temporal/angular gyrus	972
−44	−66	30	Left	Superior temporal/angular gyrus	5,211
50	−31	20	Right	Inferior parietal cortex (BA 13)	405
−29	20	47	Left	Superior frontal gyrus (BA 8)	3,726

Table S5. Independently selected regions used for task-based functional connectivity analyses across the three networks

x	*y*	*z*	Hemisphere	Anatomical landmark
FP seeds				
30	−61	39	Right	Intraparietal sulcus
−31	−59	42	Left	Intraparietal sulcus
41	3	36	Right	Middle frontal gyrus
−41	3	36	Left	Middle frontal gyrus
10	−69	39	Right	Precuneus
−9	−72	37	Left	Precuneus
51	−47	42	Right	Inferior parietal lobule
−51	−51	36	Left	Inferior parietal lobule
43	22	34	Right	Dorso-lateral prefrontal cortex
−43	22	34	Left	Dorso-lateral prefrontal cortex
0	−29	30	Midline	Midcingulate
Default-mode network seeds				
−2	−36	37	Left	Posterior cingulate
3	−51	8	Right	Retro-splenial cortex
53	−67	36	Right	Lateral parietal cortex
−47	−67	36	Left	Lateral parietal cortex
1	54	21	Midline	Anterior medial prefrontal cortex
−3	39	−2	Midline	Ventral medial prefrontal cortex
17	37	52	Right	Superior frontal gyrus
−14	38	52	Left	Superior frontal gyrus
65	−17	−15	Right	Inferior temporal lobe
−61	−33	−15	Left	Inferior temporal lobe
25	−26	−14	Right	Parahippocampal gyrus
−22	−26	−16	Left	Parahippocampal gyrus
CO network seeds				
−1	10	46	Left	Dorsal anterior cingulate cortex
36	16	4	Right	Insular cortex
−35	14	5	Left	Insular cortex
27	50	23	Right	Anterior fronto-polar cortex
−28	51	15	Left	Anterior fronto-polar cortex
10	−15	8	Right	Anterior thalamus
−12	−15	7	Left	Anterior thalamus